Improved Charge Amplification in Liquid-Metal Microfluidic Portable Energy Transducer (LIMMPET)

S. MacKenzie[1], A. Eden[1], M. Prichard[2], B. Dutcher[1], C. Meinhart[1], D. Huber[1], M. T. Napoli[1], D. Weld[2], S. Pennathur[1]
1. Department of Mechanical Engineering, University of California Santa Barbara, Goleta, CA, United States
2. Department of Physics, University of California Santa Barbara, Goleta, CA, United States

Introduction

Over the past several decades, the proliferation of portable electronic devices has driven demand for lightweight, portable energy storage. Due to the need for sustained electrical energy and the current inadequacy of batteries, there has been increased interest in energy harvesting devices, particularly for military and space applications. Energy harvesting is advantageous over traditional energy storage and delivery because the lifetime of operation is indefinite as opposed to finite. Recently, there has been much work on energy harvesting devices; however, these technologies are typically hampered by fragility, low efficiency, and often require narrow frequency ranges for operation [1-2]. We present herein the improved LIquid-Metal Microfluidic Portable Energy Transducer (LIMMPET), which utilizes alternating droplets of conductive and non-conductive fluids in a microfluidic architecture to convert hydraulic energy to electrical energy at a theoretical efficiency of >95% [3]. Liquid metals have previously been used in energy harvesting devices which leverage reverse electrowetting [4,5], triboelectric [6], electromagnetic [7], or electret-droplet interaction [8] phenomena. Building upon these approaches, we demonstrate a liquid-state Wimshurst machine which directly transduces hydraulic energy into electrical energy without the need for moving mechanical parts. The Wimshurst influence machine, which was originally developed in the 19th century, have been routinely used to generate high voltages in, for example, particle accelerators [9]. The Wimshurst machine operates by electrostatic induction to drive amplified charge separation across electrode brushes connecting isolated conducting disks that are attached to two counter-rotating wheels. The LIMMPET replaces the counter-rotating wheels and charge-carrying disks with parallel microfluidic channels populated with alternating droplets of insulating and conductive liquids. The microfluidic architecture of the LIMMPET allows for miniaturization, parallelization, and flexibility in the design and application of its energy harvesting technology. Moreover, its straightforward input parameter (pressure) allows the LIMMPET to be matched to a variety of environmental mechanical energy sources. Previous efforts using a PDMS-glass prototype have successfully demonstrated the LIMMPET's theory of operation [3]. In the current work, we develop a numerical model using the finite element package COMSOL Multiphysics 5.4 to investigate the design and assess avenues for improving the microfluidic architecture, with the ultimate goal of achieving increased charge amplification.

In Section II of this manuscript, we present the theory of operation for a microfluidic Wimshurst machine. In Section III, we present the numerical model developed in COMSOL Multiphysics 5.4, including the mathematical framework and governing equations that describe the physical phenomena exhibited in the LIMMPET. In Section IV, we present results and, finally, draw conclusions from this work, examine its potential implications, and describe future directions in Section V.

Theory

The LIMMPET operates through electrostatic induction, which promotes charge separation across two liquid metal droplets that are electrically connected through a static electrode brush. Figure 1 (left panel) depicts a schematic of the original LIMMPET device and (right panel) shows one cycle of operation. Briefly, the process begins when either 1) charge is seeded on a droplet via the jumpstart electrode, or 2) spurious charge exists on one of the flowing liquid-metal droplets. This charged droplet drives charge separation via electrostatic induction in two initially neutral liquid-metal droplets that contact the ends of a charge brush electrode in the adjacent channel segment. As these droplets flow through the microfluidic channel, they eventually break the electrical connection with the electrode brush but still maintain their induced charge imbalance. Charge is then collected from these discretely charged droplets by collection electrodes which are connected to a capacitor for storage and later use. To quantify the

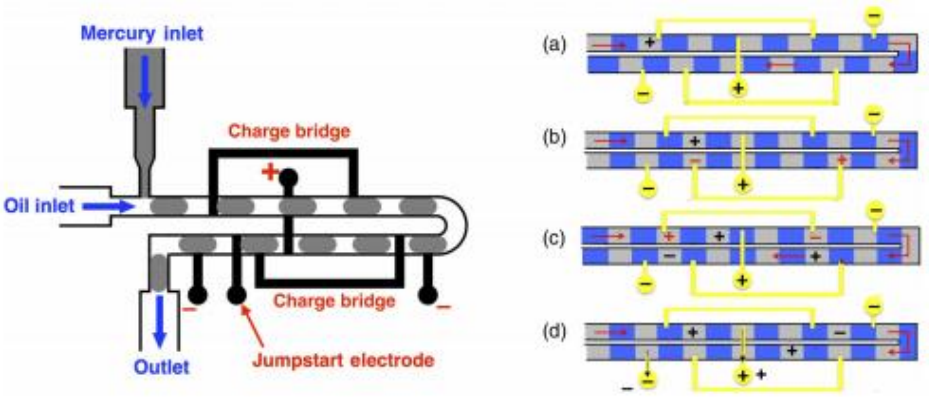

Figure 1. Schematic of original liquid-metal microfluidic energy harvester device (left panel). Liquid-metal droplets in adjacent channels capacitively interact, resulting in charge separation and amplification of initial charge inhomogeneities. The collection electrodes, labelled "+" and "-", draw charge from the droplets to a capacitor for storage and later use. The rate of voltage accumulation on the capacitor is theoretically exponential if the charge amplification factor, $\Gamma > 1$ (right panel). (a) A liquid metal droplet acquires or is given a net charge. (b) The charged droplet interacts capacitively with droplets in the adjacent channel and causes charge separation between two droplets when connected via a charge brush. As the droplets break the electrical connection with the charge brush, they maintain their separated charge and become discretely charged. (c) In the next step, the now-charged droplets continue the process by influencing droplets in contact with a charge brush in the adjacent channel. (d) Charge is extracted from the droplets when they pass over a collection electrode connected to a capacitor.

efficacy of operation, we define the charge amplification factor, $\Gamma = {q_f}/{q_i}$, as the ratio of the induced-charge on a conducting droplet q_f to the charge of the inducing droplets q_i. It is possible to analytically calculate Γ for simplified configurations using a Maxwell capacitance matrix. Theoretically, the voltage accumulation rate across the capacitor should be exponential if $\Gamma > 1$ and linear if Γ is equal to or less than unity. Previous work using a PDMS-glass prototype demonstrated linear voltage growth for a calculated charge amplification factor of $\Gamma \cong 0.4$ [3].

Numerical Model

The numerical simulations were performed using COMSOL Multiphysics 5.4 finite element simulation software in order to solve the transient charge distribution as well as quasi-static electric field during a charge induction step. We developed models with several geometric iterations to explore the effect of key parameters – namely, inter-channel spacing, curvature, and channel width ratio – on the charge amplification factor. For each microfluidic geometry, a 2D component matching the electrical architecture of the LIMMPET was imported into COMSOL directly from the lithographic masks used for microfabrication. Our model couples charge conservation from the Electric Currents interface (AC/DC module) to the Laminar Two-Phase Flow (CFD module) equations. In this manner, we implement a phase field formulation to define the interface between the conducting and insulating materials. To demonstrate the numerical model, Figure 2 shows the entire computational domain with overlaid mesh elements and boundary conditions (top) along with the Current Source domains, space charge density integration domains, and fine mesh elements near the phase field interfaces. The phase field governing equations are presented below in (1),

$$\begin{cases} \frac{\partial \phi}{\partial t} + \mathbf{u} \cdot \nabla \phi = \nabla \cdot \frac{\gamma \lambda}{\epsilon_{\mathrm{pf}}^2} \nabla \psi, & \phi = \mathrm{phipf} \\ \psi = -\nabla \cdot \epsilon_{\mathrm{pf}}^2 \nabla \phi + (\phi^2 - 1)\phi + \frac{\epsilon_{\mathrm{pf}}^2}{\lambda} \partial \mathrm{f}/\partial \phi\,, & \psi = \mathrm{psi} \\ \lambda = \frac{3\epsilon_{\mathrm{pf}}^2 \sigma}{\sqrt{8}}, & \gamma = \chi \epsilon_{\mathrm{pf}}^2 \end{cases} \quad (1)$$

where ϕ is the phase field variable, ψ is the phase field help variable, $\mathbf{u}$ is the velocity field for advection, γ is the mobility, λ is the mixing energy density, ϵ_{pf} is the interface thickness, f is the user-defined free energy, σ is the surface tension coefficient, and χ is the mobility tuning parameter. The evolution of the phase field variable is governed by the *Cahn-Hilliard equation* [10] which introduces, in addition to interfacial tension and contact angle, two other variables: the mobility parameter and interface thickness. We assume a contact angle of 90 degrees here for simplicity. The interface thickness is chosen to be no less than half of the maximum element size along the interface, while the mobility tuning parameter is set to a very small value for quasi-static droplet charging simulations; in these initial simulations used to characterize Γ, we manually place droplets at predefined locations and simply model charge induction as a quasi-static process with respect

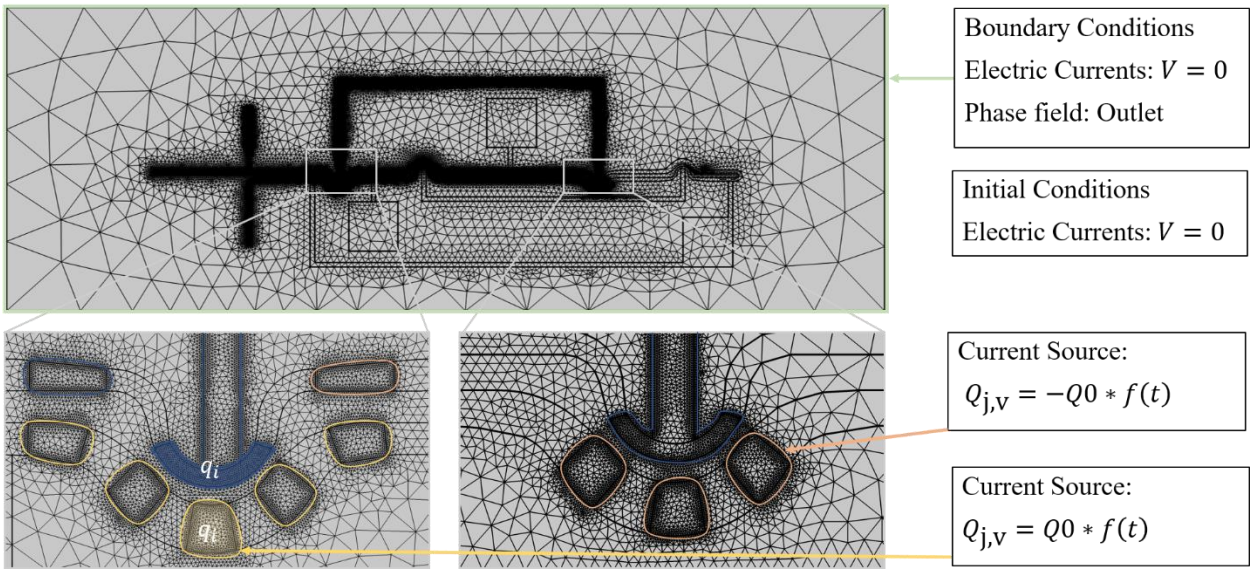

Figure 2. Diagram of the numerical mesh, boundary conditions, and current sources used in the COMSOL Multiphysics simulation. Approximately 260,000 elements were used to adequately resolve the phase field interfaces and subsequent charge accumulation. The space charge density is integrated over the regions q_f and q_i in order to calculate the charge amplification factor, $\Gamma = q_f/q_i$.

to bulk advective transport. Table 1 lists several important parameters associated with the phase field. Charge transport throughout the entire domain is modeled using the Electric Currents equations which are presented below in (2),

$$\begin{cases} \nabla \cdot \boldsymbol{J} = Q_{j,v} \\ \boldsymbol{J} = \sigma \boldsymbol{E} + \frac{\partial D}{\partial t} \\ \boldsymbol{E} = -\nabla V \end{cases} \quad (2)$$

where $\boldsymbol{J}$ is the current density vector, $Q_{j,v}$ is the charge, $\boldsymbol{E}$ is the electric field vector, σ is the surface charge density, D is the electric displacement field, and V is the electric potential. Due to the nonuniform current densities induced within the two phases by interactions with charged droplets, charge accumulates at this diffuse interface. It is necessary to use the Electric Currents interface (instead of the Electrostatic Interface, for example) because finite, albeit very low, electrical conductivity throughout the insulating phases makes charge conservation inherently dynamic; that is, there exists some finite charge transport (including charge leakage) throughout the domain for all times. Due to the massive disparity in material properties (e.g. ~15 orders of magnitude for the electrical conductivity) between the two phases, we model the phase-dependent electrical properties as varying exponentially across the phase boundary. The charged droplets are initially at zero electric potential, and a domain current source is used to briefly inject charge into each initially charged droplet for 800 ns. As it accumulates at the phase boundary, this injected charge generates an electric field in the insulating phase which polarizes and segregates charge on the two charge-bridge-contacting droplets. Some important material properties for the oil and mercury phases are listed in Table 2.

Table1. Phase Field Model Parameters

Parameter	Value
Maximum mesh element size	20 um
ϵ_{pf}	10 um
σ	38 mN/m
χ	10^{-8} m·s/kg
$\partial f/\partial \phi$	0 J/m^3

Table 2. Material Properties

Material	Oil	Mercury
Density	1.766 g/cm^3	13.55 g/cm^3
Viscosity	1.55 cP	1.5 cP
Relative Permittivity	2.09	1
Conductivity	10^{-11} S/m	104384 S/m

Results and Discussion

As previously alluded to, our model assumes that the charge induction step occurs much faster than the motion of droplets throughout the device, such that the advective transport and charge conservation are effectively decoupled. Therefore, the COMSOL Multiphysics model is solved by a three-step solution method. The first step solves the Phase Initialization for the Phase Field only. The second step solves the

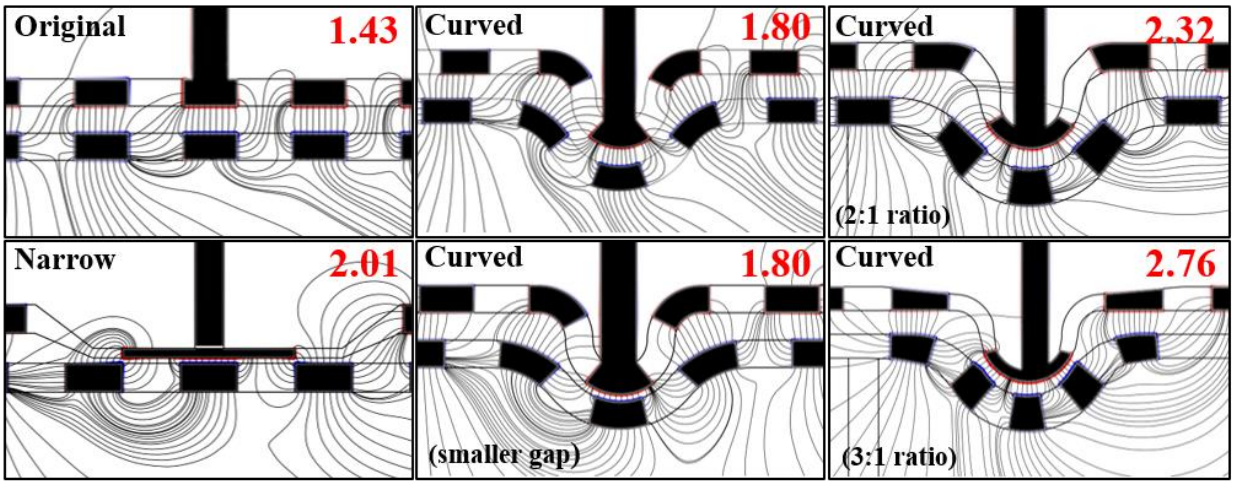

Figure 3. 2D COMSOL Multiphysics model of the LIquid-Metal Microfluidic Portable Energy Transducer (LIMMPET) design space. The charge amplification factor (shown in red) was calculated for each model to evaluate the design's effectiveness and to examine the influence of channel separation distance, channel width, and curvature. The curved geometry with the greatest channel width ratio yields the highest predicted charge amplification factor. Positive and negative space charge density are shown in red and blue, respectively, while electric field lines are shown in black.

time-dependent Phase Field evolution over a short time to obtain a stable phase field solution for the predefined droplet locations. Finally, the Electric Currents interface is solved for using the Phase Field study solution to define the electrical properties associated with the different phases. This final transient charging study is solved over 1 μs with a time step of 20 ns; this solution method requires around 6000 s to solve the three study steps.

Several microfluidic configurations were modeled within COMSOL to determine the geometry with the most effective charge amplification. The configurations tested were designed to investigate the effect of channel separation distance, curvature, and channel width ratio. Domains surrounding each conducting droplet were added and the space charge density was integrated over each domain to calculate the total charge residing at the phase interface of each droplet. Results of these calculations are shown in Figure 3, which portrays the electric field lines emanating from each droplet (black), the space charge density distribution (red and blue), the phase field variable (black and white), and the predicted charge amplification factor (red). From Figure 3, it is evident that the curved channel with the greatest channel width ratio yields the highest charge amplification factor. This is because of the physical significance of the channel width ratio; by narrowing the channel in the location where the initially neutral droplet interacts with charged droplets, this neutral droplet must stretch from an initial length of 600um to almost 1200 um to conserve volume. This elongated droplet increases the available surface area that capacitively interacts with the charged droplets in the adjacent channel segment. Conversely, by increasing the channel width in the adjacent channel, the droplets must become shorter in length. These droplets contract from an original length of around 600um in the straight portions of the channel to around 500um in the curved portion of the channel. By increasing the channel width ratio to 3:1, we therefore increase the ratio of the induced droplet length to inducing droplet length by more than 140%, allowing for a greater number of charged droplets to interact with the initially neutral droplet at any given time. We can clearly see this effect by comparing **Γ** for the "Curved", "Curved 2:1", and "Curved 3:1" geometries which are nearly identical in shape except for the channel width ratio. The simulation results also suggest that adding curvature to the microfluidic channels promotes a closer and more orthogonal capacitive coupling of droplets, which is evidenced by the denser distribution of field lines (as well as the number of field lines that terminate at the induced-charge droplet). For example, we see that by

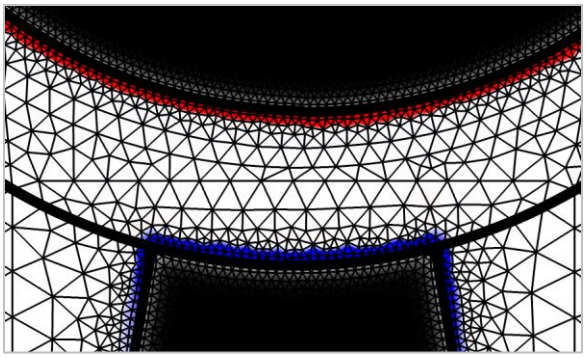

Figure 3. The volume fraction, space charge density distribution, and numerical mesh in the "Curved 3:1" model.

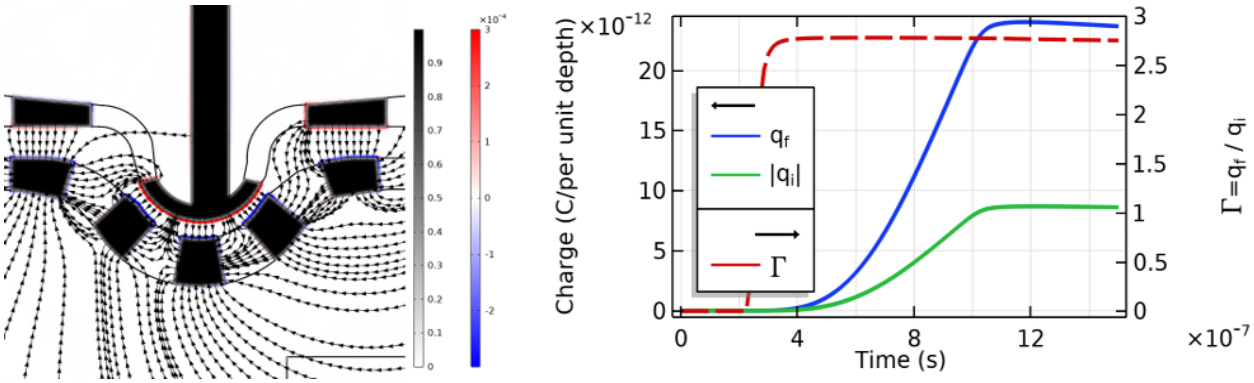

Figure 5. (Left) The positive (red) and negative (blue) space charge density and quasi-static electric field lines are plotted. There is significant redistribution of charge along the phase boundaries in the two channels. The liquid-metal phase volume fraction is also plotted as black ($\phi = 1$) for the conductor and white ($\phi = 0$) for the insulating medium. (Right) Line plot showing the time-dependent charge accumulation on top and bottom droplets (blue and green, respectively) and calculated charge amplification factor, Γ (red). Γ is recorded at ($t = 1.5 \times 10^{-6}\ s$) for reference.

comparing the "Curved" to the "Prototype" geometry, which are identical except for the curvature, $\boldsymbol{\Gamma}$ is increased from 1.4 to 1.56 due to the enhanced interaction. Lastly, we see by comparing the "Curved" to the "Curved-smaller gap" models that the channel separation distance counterintuitively has very little effect on charge amplification for the curved architecture, as both predict $\boldsymbol{\Gamma = 1.56}$. This is because although the narrowing of the gap brings the centered droplets containing $\boldsymbol{q_f}$ and $\boldsymbol{q_i}$ closer together, it simultaneously moves the two neighboring inducing droplets slightly farther from the $\boldsymbol{q_f}$ droplet; the net effect of this is to provide essentially equivalent interaction strengths.

To demonstrate the accumulation of charge in our 2D phase field models, Figure 4 depicts a 2D surface plot of the space charge density overlaid with the numerical mesh discretization. From this plot we see phase field and charge distribution transition smoothly across the conductor-insulator phase interface. A 2D surface plot of the space charge density along with the electric field lines is presented in Figure 5 (left panel). We can see from the figure that negative charge accumulates on the upper edge of the lower channel conducting droplets while positive charge accumulates in the droplet of interest in the upper channel. To the left of this induced-charge droplet, an uncharged (and electrically floating) liquid-metal droplet provides undesirable partial electromagnetic shielding of the field emanating from the inducing droplets. Furthermore, an already-charged droplet from the prior charge induction step also noticeably interferes with the induction process and causes charge leakage through the dielectric material between adjacent channels; additional design alterations to isolate the induced-charge droplet from neighboring droplets will further increase $\boldsymbol{\Gamma}$. There is equivalent charge separation and accumulation occurring at the opposite end of the charge brush, which is not depicted here. It should be noted that due to the two-dimensional nature of the finite element model, an unrealistically large capacitance is attributed to the charge brush that connects the two liquid-metal droplets. Because of this, there is some finite charge accumulation along the boundaries of the charge brush. In reality, the capacitance of the charge brush is so small compared to that of the liquid-metal droplet that almost no free charge resides on the brush. Therefore, we expect that this model underestimates the amount of charge accumulation with respect to this effect.

The charge amplification factor is calculated for all time steps in the time-dependent study and is shown along with the charge on an inducing and induced-charge droplet in Figure 5 (right panel).

Conclusions

In this paper, we introduced a 2D finite element model using COMSOL Multiphysics to numerically investigate and improve the charge amplification mechanism in the LIMMPET. Our model implements a time-dependent, phase field formulation coupled to electric currents to model charge transport throughout the device domain during a quasi-static charge induction process. The development of several models with different geometric configurations enabled us to probe the effect of channel separation distance, channel width, and curvature on the charge amplification factor. We found that the charge amplification factor is most strongly dependent on the ratio of channel widths between the charged and initially neutral droplet carrying channels, as this allows for enhanced capacitive interaction between the

(uncharged) target droplet and multiple charged droplets in an adjacent channel segment. We numerically determined a charge amplification factor of $\boldsymbol{\Gamma = 2.76}$ for the highest performing geometric design, which constitutes an improvement of greater than 5.75X compared to the original design and a factor of 2X greater than the initially proposed improved design that was developed without the aid of COMSOL Multiphysics.

References

1. C. Wei, X. Jing, A comprehensive review on vibration energy harvesting: Modelling and realization, *Renewable Sustainable Energy Review*, **74**, 1 (2017)
2. H.B. Radousky, H. Liang, Energy harvesting: An integrated view of materials, device and applications, *Nanotechnology*, **23**, 502001 (2012)
3. C. Conner, T. de Visser, J. Loessberg, S. Sherman, A. Smith, S. Ma, M. T. Napoli, S. Pennathur, D. Weld, Energy Harvesting with a Liquid-Metal Microfluidic Influence Machine, *Physical Review Applied*, **9**, 044008 (2018)
4. T. Kupenkin, J.A. Taylor, Reverse electrowetting as a new approach to high-power energy harvesting, *Nature Communications*, **2**, 448 (2011)
5. T.H. Hsu, S. Manakasettharn, J.A. Taylor, T. Krupenkin, Bubble: a novel ultra-high power density energy harvesting method based on reverse electrowetting, *Scientific Reports*, **5**, 16537 (2015)
6. W. Tang, T. Jiang, F.R. Fan, A.F. Yu, C. Zhang, X. Cao, Z.L. Wang, Liquid-metal electrode for high-performance triboelectric nanogenerator at an instantaneous energy conversion efficiency of 70.6%, *Advanced Functional Materials*, **25**, 3718 (2015)
7. S. Guo, P. Wang, J. Zhang, W. Luan, Z. Xia, L. Cao, Z. He, Flexible liquid metal coil prepared for electromagnetic energy harvesting and wireless charging, *Frontiers in Energy*, Online First (2019)
8. Z. Yang, E. Halvorsen, T. Dong, Electrostatic energy harvester employing conductive droplet and thin-film electret, *Journal of Microelectromechanical Systems*, **23**, 315 (2014)
9. A.W. Simon, Quantitative theory of the influence electrostatic generator, *Physical Review*, **24**, 690 (1924)
10. J.W. Cahn, J.E. Hilliard, Free energy of a nonuniform system. I. Interfacial free energy, *Journal of Chemical Physics*, **28**, 258 (1958)

Acknowledgements

This material is based upon work supported by the National Aeronautics Space Administration under Contracts No. NNX16CS10P and No. NNX14CS61C, awarded to Angstrom Designs, Inc. The content of the information does not necessarily reflect the position of the policy of the Government, and no official endorsement should be inferred. A portion of this work was performed in the UCSB Nanofabrication Facility, an open access laboratory.